https://doi.org/10.15407/ufm.27.01.130

S.M. VOLOSHKO [1,*], B.M. MORDYUK [2,], M.O. VASYLYEV [2,***], and A.P. BURMAK [1]**

[1] National Technical University of Ukraine
'Igor Sikorsky Kyiv Polytechnic Institute',
37 Beresteiskyi Ave., UA-03056 Kyiv, Ukraine

[2] G.V. Kurdyumov Institute for Metal Physics of the N.A.S. of Ukraine,
36 Academician Vernadsky Blvd., UA-03142 Kyiv, Ukraine

[*] voloshkosvetlana13@gmail.com, [**] mordyuk@imp.kiev.ua, [***] vasil1934@ukr.net

MICROSTRUCTURE AND FATIGUE BEHAVIOUR OF AlSi10Mg ALLOY SAMPLES FABRICATED BY SELECTIVE LASER MELTING

The review consolidates state-of-the-art research on the AlSi10Mg alloy, specifically focusing on the samples produced by selective laser melting (SLM). Currently, SLM is the most promising technique among the emerging additive-manufacturing (AM) technologies used for printing AlSi10Mg-alloy parts in industrial applications such as aerospace and automotive. The more specific goal of this study is to analyse how the fatigue behaviour of printed AlSi10Mg-alloy samples by SLM is influenced by printing parameters and post-processing treatments, in order to improve product quality under conditions of exposure to vibrations of different frequencies and intensities. It is important to note that the fatigue performance properties of the SLM-produced parts are evaluated according to the relative bulk and surface microstructures and defects' criteria. The following printing parameters are analysed: laser power, layer thickness, scanning speeds, hatch distances, platform temperature, and printing orientation. Additionally, the review examines post-processing treatments enhancing fatigue resistance. These ones include heat treatment (age hardening and stress relief), friction stir processing, hot isostatic pressing, stream finishing process, and shot peening. The fatigue behaviour is compared for the as-printed and surface-modified samples. Furthermore, the impact of these treatments on the alloy microstructure, particularly, the distribution and morphology of the Si phases within the aluminium matrix, is critically discussed, as they influence fatigue.

Keywords: additive manufacturing, microstructure, fatigue, aluminium alloys, selective laser melting.

Citation: S.M. Voloshko, B.M. Mordyuk, M.O. Vasylyev, and A.P. Burmak, Microstructure and Fatigue Behaviour of AlSi10Mg Alloy Samples Fabricated by Selective Laser Melting, *Progress in Physics of Metals*, **27**, No. 1: 130–156 (2026)

1. Introduction

It is known that engineering structures and parts are frequently subjected to cyclic loads. Such loads induce the cyclic stresses within the material, which result in the microscopic and macroscopic degradation of the mechanical properties and the physical damage. This phenomenon occurs even when the gross stresses are well below the material's ultimate strength. This process of damage accumulation in the materials due to cyclic loading is known as 'fatigue' [1–6].

In general, fatigue is the problem that affects any structural component or part that moves. As the examples aircraft (principally the wings) in the air, nuclear reactors and turbines under cyclic temperature conditions (*i.e.*, cyclic thermal stresses) are those in which the fatigue behaviour of the material assumes singular importance. It was estimated that 60–90% of the service failures of the metallic components that undergo movement of one form or another could be attributed to fatigue failure. Following this observation, some pioneering work performed by August Wöhler on the failure of the locomotive axles laid the foundation for the understanding of fatigue. Wöhler plotted the Krupp axle steel data *versus* stress (S) and the number of cycles to failure (N). This plot was later named the S–N diagram [7]. The S–N diagram is useful for forecasting the fatigue life and endurance limit of metals, *i.e.*, the limiting threshold value of the stress below which the engineering material exhibits a high or infinite fatigue life.

The study of fatigue behaviour encompasses several aspects: the fatigue stress cycle, the S–N curve, the existence of fatigue limits, and the fracture mechanisms under cyclic loading. Understanding of the fatigue mechanisms is essential for predicting the service life of components and for developing strategies to mitigate failure risks. Fatigue failures occur in three stages. These are crack initiation (currently crack nucleation is the preferred term), growth in the crack size during its progression through the metal and final fracture. The latter stage is known as a fast fracture because it occurs almost instantaneously when there is too little of the metal remaining to support the applied load.

Fatigue is known to be the process of initiation and propagation of cracks in the material due to the cyclic loading. Once the fatigue crack has initiated, it grows a small amount with each loading cycle, typically producing striations on some parts of the fracture surface. The crack will continue to grow until it reaches the critical size, which occurs when the stress intensity factor of the crack exceeds the fracture toughness of the material, producing rapid propagation and typically complete fracture of the structure. Tensile stresses nucleate and grow fatigue cracks. Compressive stresses slightly resist nucleation and retard growth. Surface roughness accelerates the cracks' initiation but does not affect their propagation. Cold working, conversely retards initiation but may accelerate propagation [8].

Generally, fatigue cycles can be classified into the categories, which follow below [7].

• High-cycle fatigue, also called 'stress-controlled fatigue', involves conducting fatigue tests using the prescribed cycle of fixed load or stress limits. This type of fatigue generally occurs with high-stress cycle numbers ($<10^4$ cycles).

• Low-cycle fatigue, termed "strain-controlled fatigue," involves conducting the fatigue tests using the prescribed set of elastic and plastic strain limits within each cycle. This type of fatigue occurs at low numbers of stress cycles ($<10^3$ cycles).

• Ultra-low cycle fatigue. This section highlights the unique characteristics of ULCF, such as its occurrence under large cyclic loads leading to complete ductile fracture and the distinct mechanisms involved, which are different from those in HCF and LCF.

• Ultra-high cycle fatigue (UHCF), which refers to the phenomenon of fatigue failure that occurs at extremely high numbers of cycles, typically exceeding 10^7 or even 10^9 cycles. Key factors influencing fatigue behaviour include the material's microstructure, the presence of stress concentrators, surface finish, mean stress, frequency of loading, and environmental conditions.

Currently, the study and improvement of the fatigue resistance of parts obtained by additive manufacturing (AM) have become a very important task [9–12]. Over the last few decades, AM has represented the major innovation in the production of engineering components, enabling the production of parts with complex geometries and lightweight structures that are difficult to achieve as compared to traditional subtractive manufacturing methods. Laser powder bed fusion, typically layer by layer as one of the widely used AM technologies, has gained considerable attention to fabricate a variety of metal alloy parts with novel microstructure and properties to various industries, including the automotive, the aerospace, turbine palettes, and the medical implants. Regarding the industrial applications, in recent years, AM components have become widespread in applications in which static loads are applied, whereas their use is still limited in cyclic loads. It was established that the fatigue response of as-built or heat-treated AM parts is generally worse than that of traditionally built parts, thus preventing their diffusion in sectors where high safety standards are required, particularly in the aerospace and automotive sectors. According to the literature, many factors are responsible for the weaker fatigue response of AM parts. Among these, the surface roughness, anisotropic properties, the highly directional columnar grain structures, pores and inclusions play a significant role in the fatigue behaviour. For these reasons, one of the main challenges for researchers is to extend the knowledge of the response of AM parts and the mechanisms of the crack initiation and propagation, to propose conservative design methodologies capable of preventing the fatigue failures of AM parts.

The production of aluminium alloys by powder bed fusion AM methods has become widespread due to the ease of processing with the laser-based systems, due to the low melting point and eutectic composition of this alloy. The excellent properties of these materials, such as the high corrosion resistance, strength-to-weight ratio, and low thermal expansion, have recognised the AlSi10Mg alloy in the Al–Si–Mg system as highly demanded for many applications in aerospace, automotive industries and heat exchanger products. This hypoeutectic alloy is near the eutectic typical chemical composition (wt.%): Mg — 0.2–0.45; Si — 9–11; Fe < 0.55; Cu < 0.05; Mn < 0.45; Ni < 0.05; Zn < 0.1; Pb < 0.05; Sn < 0.05; Ti < 0.15; Al — bal. The specific material properties are for this alloy: elastic modulus $E = 75$ GPa, yield stress $\sigma_т = 275$ MPa and density $\rho = 2.7$ g/cm^3 [13–15].

In conventional manufacturing, this alloy is usually produced through casting. Among the AM techniques for metals, selective laser melting (SLM) is one of the most widely used and employed to produce aluminium-based parts, particularly of AlSi10Mg alloy components. SLM offers the unique advantage over traditional casting by enabling precise adjustments in processing parameters. Recently, a lot of the research work has been focused on SLM AlSi10Mg, including process optimisation, microstructure and the mechanical properties of the complex geometric high-density parts. SLM is the additive manufacturing process where the laser source selectively scans the powder bed according to the part CAD data to be produced. The high-intensity laser beam makes it possible to completely melt and fuse the metal powder particles together to obtain almost fully dense parts. Successive layers of metal powder particles are melted and consolidated on top of each other, resulting in the near-net-shaped parts, other than surface finishing [16–18]. A schematic view of the SLM process and main components of the machine SLM are illustrated in Fig. 1 [19].

Despite the advantages of AM, there are problems, especially related to the defect formation during the layer-by-layer printing of SLM parts. These defects, often caused by variations in the laser energy, powder properties, and process parameters, can significantly influence the mechanical properties of AM components. Several types of critical defects were found: surface defects originated during the removal of the support structures, internal defects due to incomplete fusion, clusters of pores concentrated near the specimen surface, balling defects, internal voids, oxides, melted powder and the relatively rough surface. Many factors were observed to affect the defect population and the defect size, particularly, the platform heating, the scanning strategy, the SLM process and the part orientation concerning the printing direction. Together with the defect

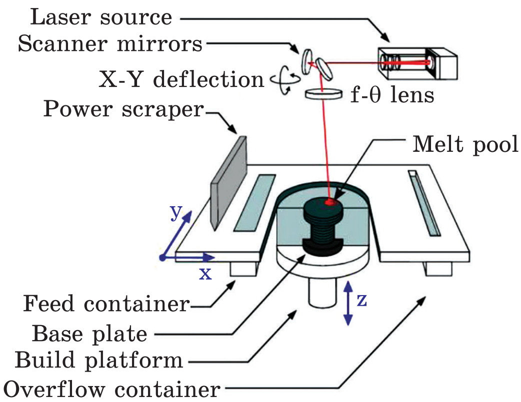

Fig. 1. Schematic overview of the SLM machine [19]

size, the microstructure and the residual stresses also play a key role [20]. These printing defects are extremely dangerous for components subject to fatigue because they represent the critical initiation site for the fatigue crack and could lead to unexpected failures.

The AlSi10Mg parts produced by selective laser melting were shown to possess residual defects like pores and oxide particles. The pores and oxide particles in AlSi10Mg parts produced by SLM were analysed in Ref. [21]. The critical role of these defects in fatigue failure was identified, and a correlation between the crack-initiating pore on the fracture surface and fatigue life was established. As shown, a good agreement was achieved between the pore size distribution measured on a 2D section of the studied samples and the fatigue life predicted using extreme-value theory. Similar conclusions were achieved in [22], where crack initiation was revealed to occur, typically, due to pores and Si particles on the surface or sub-surfaces. Additionally, the cellular structures in the microstructure played a significant role in influencing the fatigue crack path.

Either bulk heat treatments [23–28] affecting phase composition and stress state or surface deformation treatments [29–35] forming the hardened and compressed near-surface layers are generally used to improve fatigue properties of metallic materials, including the prolongation of fatigue life of additively manufactured AlSi10Mg parts. Several studies have explored the effects of defects on the fatigue behaviour of various materials, providing valuable insights into the complex relationship between defect characteristics and material performance. Depending on the heat treatment type (solution treatment or direct ageing) and chosen temperature/duration, the fatigue behaviour was reported to be deteriorated [23, 24] or enhanced [24, 26]. A superior fatigue strength of the surface-modified materials is generally supported by the lowered surface roughness as well as a high microhardness and compressive stresses in the surface layer [29–31] supported by gradient nanostructuring [32–34]. The following surface modification techniques are frequently applied: shot peening [30, 32], laser shot peening [30, 32], ultrasonic impact treatment [29, 31], ultrasonic surface rolling process [33, 34], and severe vibratory peening [32].

The results of this study underscore the importance of controlling both defect characteristics and printing direction to optimise the fatigue behaviour of the SLM parts. A further factor that is likely to affect the performance of the SLM-produced parts is post-process surface treatment. These problems are addressed in this review concerning the AlSi10Mg alloy.

2. Printing Directions

The effect of the printing directions on the fatigue properties was studied in [36]. The samples manufactured in the different directions were fatigue tested in the peak-hardened (T6) and as-printed condition. In this experiment, the following SLM printing parameters were applied: laser beam power of 250 W; laser beam diameter of 0.2 mm; layer thickness of 50 μm; laser scanning speed of 500 mm/s; laser scanline spacing of 0.15 mm; argon gas shielding; the platform temperature was set to 30 °C. The platform heating reduces residual stresses and distortion of the printed samples. The particle size of the AlSi10Mg alloy powder was in the range of 25–45 μm. The longitudinal axis of the samples was parallel to the x–y plane at 0° and perpendicular to the x–y plane, *i.e.*, parallel to the Z-axis, at 90°. After printing, the samples were post-heat treatment T6 (Solution heat treatment for 6 h at 525 °C and the room temperature water quench; artificial ageing for 7 h at 165 °C).

The high-cycle fatigue (HCF) samples (Fig. 2) with stress concentration factor $K_t \approx 1$ were printed with material allowance (1 mm), machined according to ASTM E466 (ASTM International. Standard practice for conducting constant amplitude axial fatigue tests of metallic materials. ASTM E 466-07: ASTM International; 2007), and tested according to EN 6072 (Standard. Aerospace series–metallic materials–test methods–constant amplitude fatigue testing. DIN EN 6072: 2010; 2010) at the room temperature on the Microtron 654 (Rumul) resonance tester. The test frequency of approximately 10^8 Hz and stress ratio of $R = \sigma_{min}/\sigma_{max} = 0.1$ were used. The HCF tests were terminated at $3\cdot10^7$ cycles.

To determine the porosity, polished and unetched micrographs were investigated (Fig. 3). The porosity is visible in all printing directions, and pores generally were below 300 μm. According to the phase diagram of the Al–Si system, the microstructure of the printed samples after post heat-

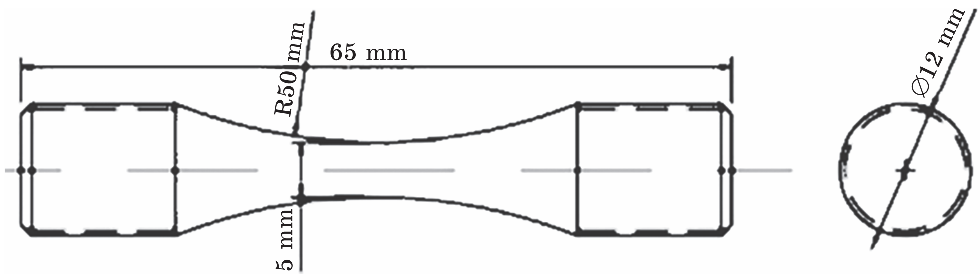

Fig. 2. High-cycle fatigue sample [36]

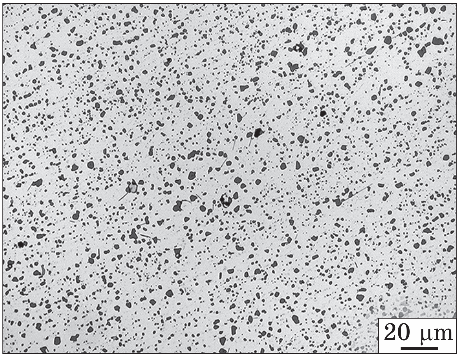

Fig. 3. Typical microstructure of fatigue sample (30 °C/0°/ peak-hardened); plane is perpendicular to the longitudinal axis of the sample [36]

treatment is characterised by the size and arrangement of such phases as the Al matrix and the eutectic Si-particles. In addition, a minor amount of the phases Mg_2Si, $A_{l9}Fe_2Si_2$, and $Al_8Si_9Mg_3Fe$ can be observed according to Ref. [37]. After peak hardening, the eutectic Si particles have coarsened and formed into a globular shape. The microstructure is homogeneous, and there is no significant microstructural difference between 0°, 45°, and 90° samples apparent. The dendrites, laser traces, and the heat-affected zones are not visible anymore.

Figure 4 shows the fatigue resistance (σ_{max}), *i.e.*, $\sigma_{max} = \sigma_{min}/0.1$, *versus* the number of cycles at 30 °C of platform temperature. It can be observed that the fatigue resistance is higher in the 0° direction than in the 45° and 90° directions.

Very-high-cycle fatigue (VHCF) behaviour of the as-printed samples without post heat-treatment was studied in Ref. [38]. To study the influence of the printing orientation on fatigue, the samples were printed with two orientations, namely vertically (90°) and horizontally (0°). The related printing parameters used by authors are laser power 370 W, scanning speed 1300 mm/s, scanning spacing 0.19 mm, preheating temperature 35 °C, powder size 0.05 mm, printing direction 0° and 90°.

For the fatigue tests, the ultrasonic fatigue-testing machine equipped with the ventilation system was used. The experimental basis of this machine is the resonance of the sample at the resonance frequency of 20 kHz. The fatigue tests were performed under displacement control in the range from 2.2 to 21.5 μm according to the stress–strain relationship, which was from 40 MPa to 390 MPa. During the experiment, the room temperature was kept.

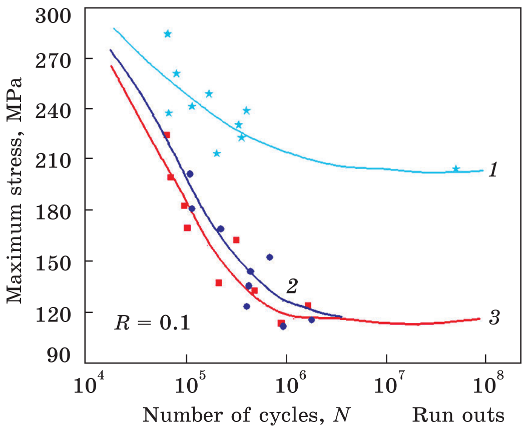

Fig. 4. Fatigue resistance and Weibull distribution (50% probability of failure) of the samples that are printed in the 0° (*1*), 45° (*2*), and 90° (*3*) directions [36]

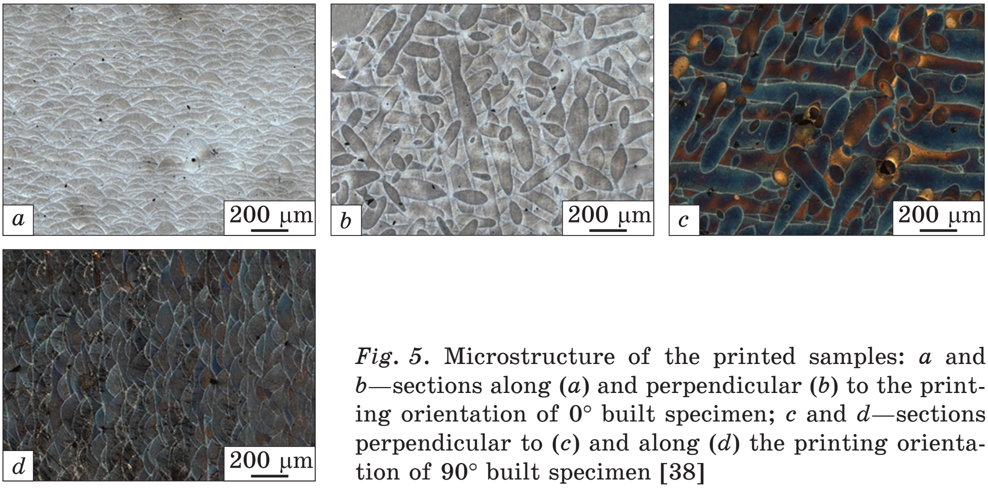

Fig. 5. Microstructure of the printed samples: *a* and *b*—sections along (*a*) and perpendicular (*b*) to the printing orientation of 0° built specimen; *c* and *d*—sections perpendicular to (*c*) and along (*d*) the printing orientation of 90° built specimen [38]

Due to material anisotropy, two types of samples built from the sections along and perpendicular to the printing orientation, *i.e.*, 0° and 90° orientations, were analysed. The optical microscopy observations of the microstructures of these two samples are shown in Fig. 5. As seen, there is no obvious difference in the microstructures between the two orientations. The section along the printing orientation shows the fish-scale appearance, which is formed during the printing process. The segments in Fig. 5, *b*, *c* are not continuous because the laser beam may penetrate the previous layer when melting. In addition, the hatch distance measured from Fig. 5, *b*, *c* is about 200 μm, which is very close to the set value of 190 μm. Therefore, it is the laser process parameters rather than the printing orientation that determines the material microstructure.

It is demonstrated by the *S*–*N* data (Fig. 6) that the printing orientation has an important effect on the fatigue property. As shown in Figure 6, the fatigue strength of the 90° printed samples is lower than that of the 0° printed ones. There are two reasons for this effect. First, different stresses act on the samples manufactured at the different orientations. The other reason may be that the defect size of the 90° built samples is larger

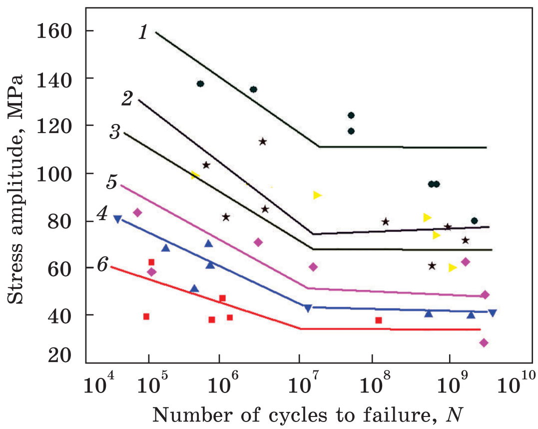

Fig. 6. The *S*–*N* data for the samples printed with different orientations and under different mean stresses: *1* — 0°, $R = -1$; *2* — 90°, $R = -1$; *3* — 0°, $R = 0$; *4* — 90°, $R = 0$; *5* — 0°, $R = 0.5$; *6* — 90°, $R = 0.5$ [38]

than that of the 0° built specimens. The variation of fatigue strength with orientation is also in agreement with that of the observed tensile strength.

3. The Post-Treatment

3.1. Heat Treatment

In Ref. [39], the influence of the two different types of post-heat treatment, *i.e.*, a standard T6 and direct ageing (DA), on the HCF behaviour was studied. First, a T6 heat treatment was applied at 520 °C for 2 h (solution heat treatment), followed by water quenching; subsequently, the material was aged at 180 °C for 6 h to obtain the T6 alloy. Second, the as-printed alloy was not subjected to the solution heat treatment described above, but the ageing treatment was carried out at 180 °C for 6 h to obtain the DA alloy. Samples of the as-printed and heat-treated samples were prepared according to ASTM, Designation: E 8M, METRIC., Standard Test Methods for Tension Testing of Metallic Materials for Fatigue Tests. The as-printed and heat-treated samples were machined to prepare plate specimens with a gauge length of 12 mm, a width of 3 mm, and a thickness of 1 mm. The fatigue tests were conducted at the ambient temperature by employing INSTRON 8501 equipment at the nominal strain rate of 10^3/s and fatigue stress frequency of 10 Hz with the stress ratio $R = 0.1$. To improve the fatigue strength's accuracy in preventing external defects, the surface was evenly polished. The fatigue limit was defined as the maximum stress at which failure does not occur once the number of cycles reaches $\cong 10^7$.

SEM images of the typical microstructures of the as printed, T6, and DA samples are shown in Fig. 7, *a*, *b*, *e*, *d*, and Fig. 7, *c*, *f*, respectively. For the as-printed sample, the molten pools and the boundaries are noticeable in Fig. 7, *a, d*. As seen, the Si precipitates are located at the boundary of the cellular structure that formed inside the molten pool. Such an effect is exhibited in general SLM-built Al–Si structures [25]. For the T6 sample (Fig. 7, *b*, *e*), such molten pools and their boundaries disappeared. It is because of the high heat-treatment temperature. The regime of the solution heat treatment has sufficient time for the segregated Si to diffuse and form particles/spheroids in addition to microstructural coarsening (circa 1.8 μm). Thus, the Si phase size is significantly coarser than that of the as-printed sample. Although the heat-treatment temperature was not very low at 180 °C, the molten pool microstructure with the cellular structure was sustained even after the conditions under which the heat treatment was applied to the DA sample (Fig. 7 *c*, *f*). Unlike the as-printed sample, a large amount of the fine Si precipitate was generated inside the cellular structure of the DA treatment. The XRD analysis showed that the T6 sample contains a higher fraction of the Si phase.

The *S*–*N* curves of the HCF fatigue test samples in Fig. 8 show the results for the maximum stresses and the number of cycles to the samples'

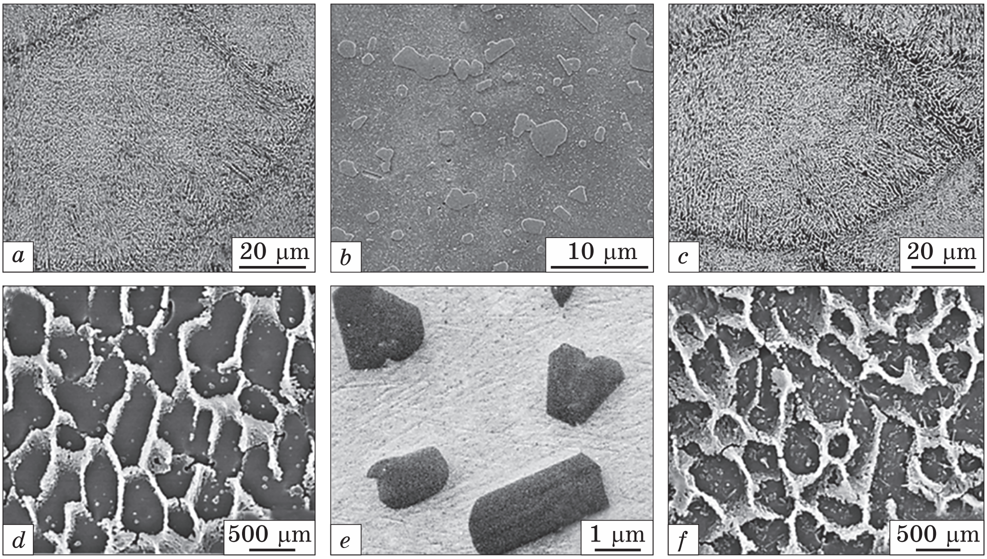

Fig. 7. Typical SEM microstructures: *a*, *d* — as-printed; *b*, *e* — T6 treatment, and *c*, *f* — DA treatment [24]

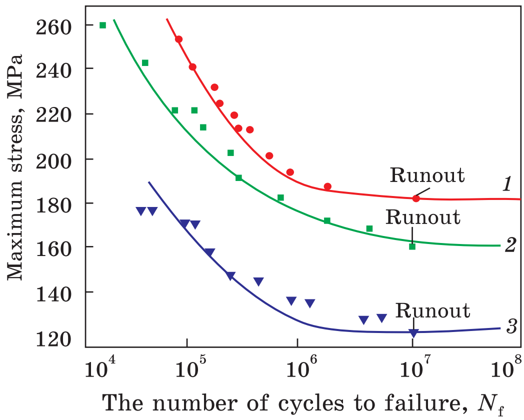

Fig. 8. Variation of maximum stress with the number of cycles: *1* — DA; *2* — as-printed; *3* — T6 treatment of the as-printed samples [24]

failure. These data indicate that the S–N data for the SLM AlSi10Mg does not exhibit the fatigue limit; thus, it was deliberately estimated. The fatigue limits determined for the as printed, T6, and DA samples are 160, 120, and 180 MPa, respectively. The fatigue limit of the DA alloy increased by as much as 20 MPa compared with that of the as-printed condition, as opposed to that of the T6 treatment, which decreased by as much as 40 MPa. These results show that under the same stress conditions, the fatigue properties of the DA alloy are superior to those of the as-printed sample. The HCF properties are proportional to the yield strength or tensile strength, as prominently stated. The fact that the material has high strength signifies that it has superior high-cycle fatigue properties as well. Likewise, as mentioned above, the heat treatment is also an important method for improving the fatigue properties.

Similarly, Uzan *et al.* reported that stress relief heat-treatment (SRHT) and hot isostatic pressing (HIP) at either 250 °C or 500 °C decreased the

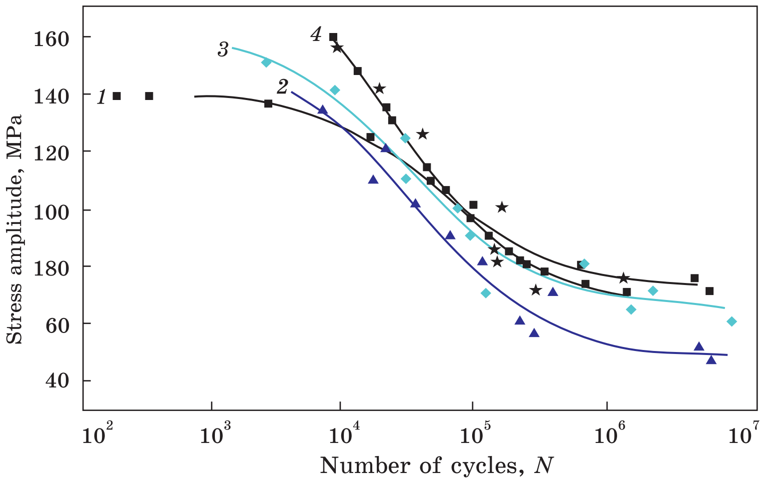

Fig. 9. The S–N curves of the four groups of samples: *1* — T300; *2* — no HT; *3* — T240; *4* — T200 [26]

yield strength, hardness, and fatigue limit of the SLM-built AlSi10Mg specimens. The SRHT and HIP treatment at 500 °C resulted in the lowest fatigue resistance due to significant microstructural changes [23].

The study [26] provides a deeper understanding of the different procedures and the heat treatment effect on the fatigue properties of SLM samples. Such information can be useful for optimising the post-process to improve the overall performance of the printed parts in practical applications. The following sample types are investigated: samples were left as printed without any additional heat treatment (NoHT); samples were subjected to the conventional heat treatment recommended by the supplier of the printing powder. The samples were heated to 240 °C and held for 6 hours, followed by cooling in air (T240); samples were heated to 200 °C for 2 hours, followed by air-cooling to the ambient temperature (T200); samples were heated to 300 °C for 2 hours, followed by water-cooling (T300). All samples were printed in the vertical direction within one printing cycle by the Concept Laser M2 printer (with printing parameters according to [39]). Four groups of samples (differing by the different heat treatment conditions) were tested, with each group consisting of 14 samples designated for fatigue experiments. Eleven samples from each fatigue-related group were used to establish the S–N curve. All samples were left with surfaces in the as-printed state; no machining (except for threaded heads) was applied. The fatigue experiments, which were conducted in this campaign, had the condition to end the experiment, when any of these limits is exceeded, namely, frequency drops by 10 Hz, load amplitude changes by ±0.5 kN, static loads change by ±0.5 kN, 10^7 cycles were reached. These samples were classified as run-outs. Such samples were then subjected to another subsequent cyclic loading with at least twice the higher load amplitude.

It can be observed in Fig. 9 that the lowest fatigue performance was exhibited by NoHT samples, which were not subjected to any heat impact. Obviously, there is no residual stress relief after printing. The performance of the samples subjected to any heat treatment is superior in all cases demonstrated in this study. Particularly, samples T200 and T240 exhibit nearly identical fatigue behaviour in the range from 1e5 to the fatigue limit level. The low-cycle fatigue region below 100 000 cycles indicates that the sample T200 show the higher fatigue strength. The T300 sample results in the highest fatigue limit. In this case, however, the worst fatigue performance is observed in the transition to the low-cycle fatigue region. This response can be attributed to the decomposition of the Si network. The lowest scatter of the experimental data was also observed for this T300 series. Overall results show us that the fatigue strength performance and the tensile performance are the best for the T300 series with heat treatment at 300 °C. It should be pointed out, however, that the T200 heat treatment leads to the best fatigue performance at the lower lifetimes below 50 000 cycles approximately.

3.2. Hot Isostatic Pressing

The study [40] aims to establish the effect of the stress relief heat treatments carried out at a temperature (250 °C) on the fatigue behaviour of SLM-printed alloy samples. It is also explored the thermomechanical impact, specifically hot isostatic pressing at a temperature of 250 °C with a pressure of 100 MPa. The fatigue performance of these two tailored heat treatments is also compared with that of both as printed and stress-relieved at 300 °C samples. The SLM processing parameters adopted were the laser power of 350 W, the scanning speed of 1800 mm/s, the hatch distance of 80 μm, the rotation increment angle of 67°, the layer thickness of 30 μm, and the printing platform temperature of 150 °C. The samples were printed in the vertical direction with standard rod-like shapes. The sample's density measured was approximately 99.969%. After the printed samples (AP) the next post-processing was used in this study: residual stress relief at 300 °C for 2 h followed by cooling in air upon removing from the furnace (SSR); residual stress relief at 250 °C for 2 h followed by water quenching (TSR); hot isostatic pressed at 250 °C under 100 MPa followed by cooling in air upon removing from the furnace (HIP). Before the fatigue testing, all samples were polished using various sandpaper grits (#600, #1200, and #2500), followed by the diamond paste. As a result, the arithmetic average roughness was $R_a =$ $= 0.207\pm0.012$ μm. The axial strain-controlled fatigue tests were conducted according to the procedures of the ASTM E606 standard. The tests were performed with the strain ratio $R = -1$, and the strain rate ($\Delta\varepsilon/\Delta t$)

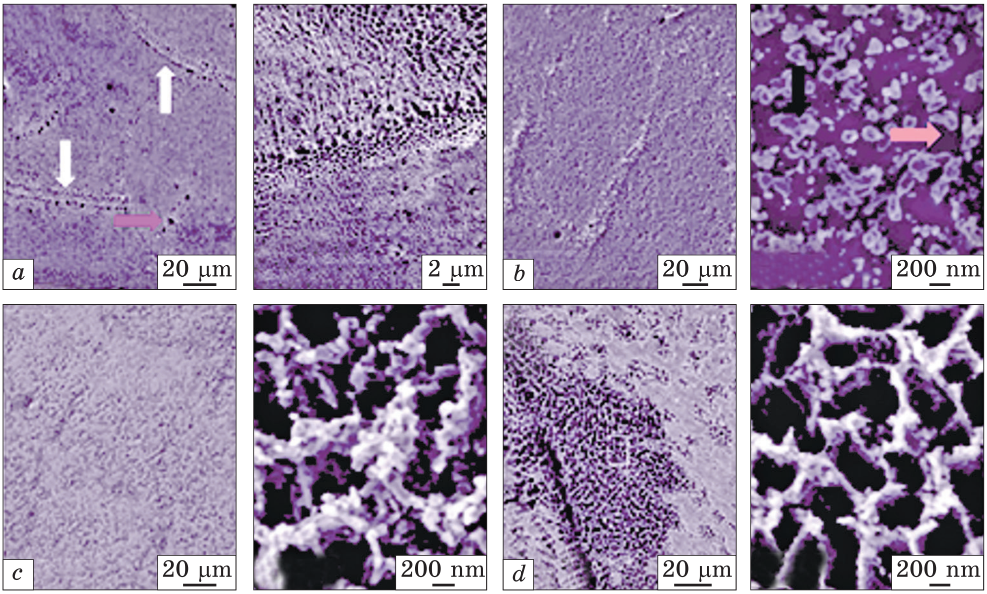

Fig. 10. Microstructure features of L-PBF AlSi10Mg aluminium alloy: (*a*) AP; (*b*) SSR; (*c*) TSR; (*d*) HIP. Left-hand side: lower magnification, right-hand side: higher magnification. The red arrow refers to insoluble gases and cavities; the white arrow refers to partial fusion resulting from laser overlap between melt pools, the yellow arrow refers to the Al matrix, and the black arrow refers to Si particles [40]

of $8 \cdot 10^{-3}$ s^{-1} with the sinusoidal waves. The strain amplitude ranged from 0.1% to 1.5%.

The microstructure of the as-printed sample is exhibited in Fig. 10, *a*. One can observe the supersaturated Si cellular-dendritic microstructure, where Al (shown in grey) is surrounded by the fibrous network of Si (shown in white). It is also possible to distinguish from the figure the different melt pool boundaries, each contributing to the formation of distinct microstructures through the solidification process associated with the various melting pools. There is also visible the porosity, which is a result of the insoluble gases and cavities (see red arrows). This can be attributed to partial fusion due to the laser overlap between the melt pools (white arrows). On the other hand, for the SSR samples (Fig. 10, *b*), it is clear that the cavities and the melting pool boundaries were removed due to the consequence of the thermal expansion and thermal contraction, as well as the migration of Si atoms. Another important feature is that such a heat treatment removed the typical cellular microstructure and the fibrous Si network associated with the as-printed samples. In this case, the microstructure is composed of the aluminium matrix represented by the grey areas (*e.g.*, yellow arrow) with the Si particles visible as the light grey areas (*e.g.*, black arrow). Figure 10, *c* shows the usual microstructure ob-

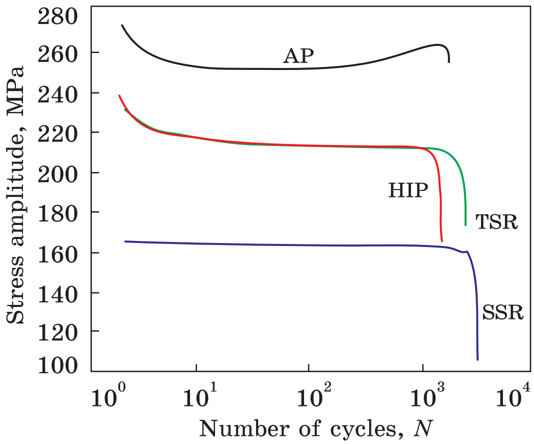

Fig. 11. Stress amplitude *versus* number of cycles to failure for the tested printed samples AP, HIP, TSR, and SSR [40]

served for the TSR samples. As seen, such a treatment led to the homogenisation of the microstructure, converting the initially fine cellular structure characteristic of the untreated alloy into a coarser cellular structure. This fact contrasts with that observed for the SSR samples. As displayed in Figure 10, *d* no significant microstructural differences were observed for the HIP samples (this HIP process was carried out at the same temperature as the TSR case). The main features are quite similar to those of the material condition subjected solely to stress relief (Fig. 10, *c*).

Strain-controlled fatigue tests. Fig. 11 plots the stress amplitude against the number of cycles for all sample states at the strain amplitudes of 0.5% (full lines) and 1.25% (dashed lines). Note that the number of cycles is plotted on a logarithmic scale for comparative purposes. Overall, the sample exhibits the saturated stage, which occupies most of the test. The initial transient stage, although it exists in some cases, occurs during a short number of cycles and is characterised by small changes. The final stage is also short, and in a few cases, the final failure occurs suddenly without any apparent reduction in the stress amplitude. Thus, in some cases, the curves obtained in the experiments did not fully show the classical three-stage response often found in conventionally manufactured states.

The following main conclusions can be drawn from the results of fatigue tests: for the SSR heat treatment the increasing fatigue strength in the low-cycle fatigue regime is observed; however, in the high-cycle fatigue regime, its performance was similar to that of the AP state; both TSR and HIP heat treatments also increased the fatigue strength in the low-cycle fatigue regime but slightly less than the SSR heat treatment and HIT had the positive effect in this regime; in the high-cycle fatigue regime, the TSR and HIP heat treatments presented different responses; without HIP, the fatigue endurance was similar to the other conditions, however, when HIP was applied, the detrimental effect was observed.

3.3. Friction Stir Processing

Friction stir processing (FSP) has been proven an effective and versatile metalworking technique for generating fine-grained microstructures and surface composites, such as modifying the microstructures of Al-based alloys and Ni–Al bronze [41–43]. In FSP, the rotating tool causes local changes in the welded material due to both the mechanical deformation and the heat generated by friction. The heat is conducted into the alloy, leading to a zone, in which the micro- (and nano-) structure of the material is significantly changed due to mechanical work and increased temperature [44] (Fig. 12). Compared to other metalworking techniques, FSP has distinct advantages. First, FSP is a short-route solid-state processing technique with one-step processing that achieves microstructural refinement, densification, and homogeneity in a single step. Second, the microstructure and mechanical properties of the processed zone can be accurately controlled by optimising the tool design [45].

In Ref. [46], FSP was used to improve the fatigue behaviour of the printed samples. The initial additive-manufactured material, in the form of $150\times35\times5$ mm plates, was produced using an EOS M290 laser powder bed fusion machine with AlSi10Mg aluminium alloy powder. The following printing manufacturing parameters were used: power, 370 W; laser advance speed, 1300 mm/s; layer thickness, 30 mm; hatch spacing, 0.19 mm. In FSP, the rotation angle between layers is 67°; the rotation speed is 1000 rpm, and the advancing speed is 500 mm/min or 1000 mm/min. The constant amplitude uniaxial tensile ($R = 0.1$) fatigue tests were performed following the ASTM E466-15 standard, on the 10 kN load cell Instron ElectroPuls E10000 test instrument, with a frequency of 30 Hz. The printed samples were machined, thus decreasing the residual stress level and its possible influence. With the same intention, the samples were mechanically polished down to $R_a = 0.1$ μm, hence avoiding the surface roughness influence on fatigue life. The tests were stopped if failure had not occurred after $2\cdot10^6$ cycles. The three samples of the following types were investigated: (*a*) the as-printed (AP), (*b*) post-heat treated (SRHT), (*c*) FSP treated at 500 mm/min (FSP500), and (*d*) FSP treated at 1000 mm/min (FSP1000).

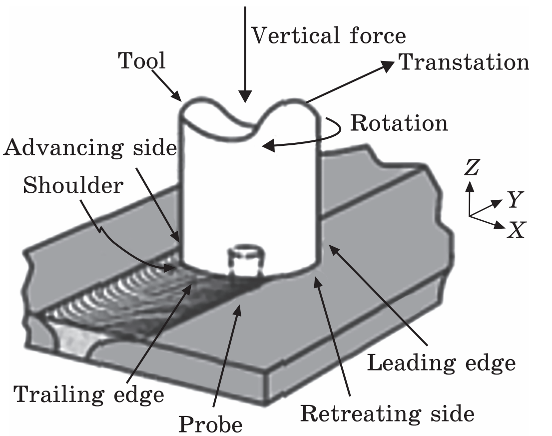

Fig. 12. Schematic illustration of the friction stir welding process [44]

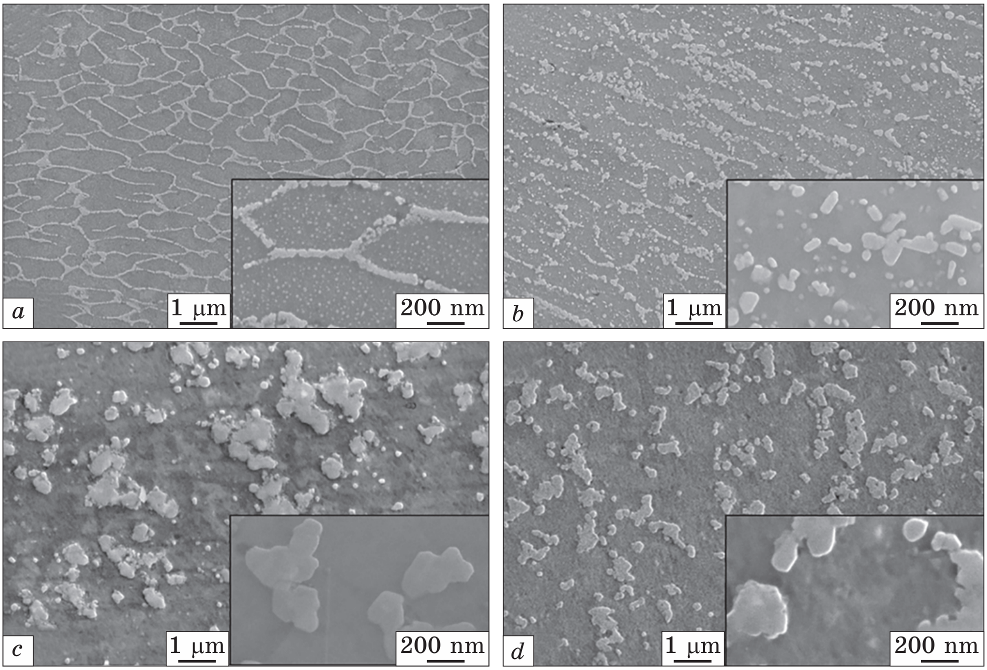

Fig. 13. SEM micrographs: AP (*a*), SRHT at 300 °C for 2 h (*b*), FSP at 500 mm/min (*c*) and FSP at 1000 mm/min (*d*) states [46]

The microstructure for the four states can be observed in Fig. 13. The AP sample presents the fine Si-rich eutectic phase forming the network surrounding the α-Al cells (see Fig. 13, *a*). The fine Si precipitates that are found inside the α-Al cells are observed. Both SRHT and FSP post-processing produce the breakdown and globularization of the Si-rich network, as can be appreciated in Fig. 13, *b*–*d*.

The fatigue *S*–*N* curves are presented in Fig. 14. The straight lines correspond to Basquin's fitting law, $\Delta\sigma = CN_f^b$, where $\Delta\sigma = \sigma_{max} - \sigma_{min}$, N_f is a number of cycles to failure, and b as well as *C* (MPa) are the material constants (Table 1).

The SRHT does not result in a significant change in total fatigue life. Contrastingly, FSP brings a very significant enhancement. Furthermore, the two different FSP parameter sets seem to yield very similar behaviour, which highlights the robustness of the process, since the significant va-

Table 1. **Parameters of Basquin's law [46]**

Parameters	AP	SRHT	FSP 500	FSP 1000
C, MPa	750	840	411	373
b	0.1	0.12	0.04	0.03

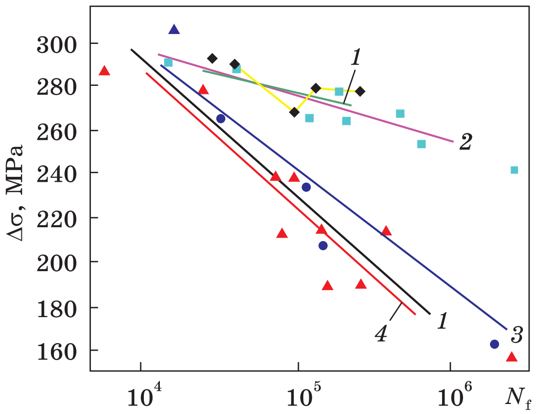

Fig. 14. The fatigue *S–N* of the failed samples: *1* — FSP 1000; *2* — FSP 500; *3* — as-printed; *4* — SRHT [46]

riation of the parameters would not compromise the total fatigue life improvement as long as they lead to defect-free material. The strength difference between FSP at 500 mm/min and 1000 mm/min is therefore limited enough to have a notable impact on the fatigue performance, so only the former was further analysed. In this case, only a limited number of Wöhler curve points (four data points) were obtained for the FSP at 1000 mm/min condition since the similarity with FSP at 500 mm/min was clearly very high, and the comparison between the various states (AP, SRHT and FSP) is already feasible.

3.4. Stream Finishing Post-Process

To improve fatigue resistance, the authors [47] proposed the stream finishing process (SFP) for post-processing of the printed sample's surface. In a first step, surface roughness evolution as well as the abrasion rate of the printed samples at the different stages of the SFP were analysed in this study. In the next step, the printed fatigue samples were post-processed by SFP and used in the rotating bending fatigue test. The results were compared with those of the samples with the turned and as printed. The following printing process parameters were used: the layer thickness was 50 μm and the focus diameter 80 μm; the laser power was 350 W; the scan speed was 1150 mm/s; the hatch offset was 0.17 mm; the platform temperature was 100 °C; the scan rotation per layer was 67°; the alloy powder size distribution was 20–63 μm. The samples were printed perpendicular to the printing platform. The schematic view of the stream finishing machine is shown in Fig. 15. The following process parameters were used for stream finishing: depth of immersion of 150 mm, radius of immersion of 250 mm, angle of immersion of 0°, rotational speed of the sample of 10 min^{-1}, rotational speed of the bowl of 70 min^{-1}. To ensure coaxial clamping during the rotating bending fatigue test, the clamping surfaces of the stream-finished and as-printed samples were turned. The cyclic behaviour of the samples was evaluated using a rotating bending fatigue test according to DIN 50113:2018-12. Loading the rotating samples with the constant bending moment results in the mean stress $\sigma_m = 0$ MPa or the stress ratio R, giving the bending fatigue strength σ_f.

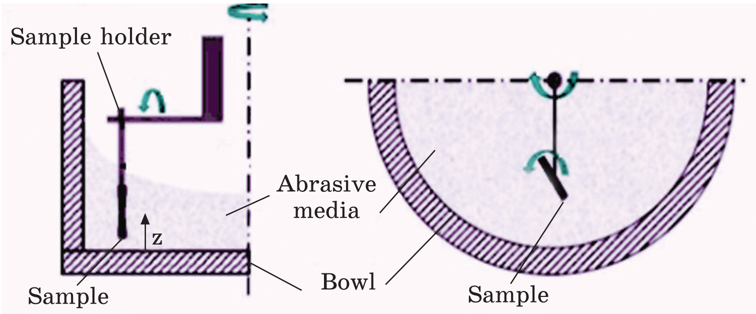

Fig. 15. Schematic view of the stream finishing machine [47]

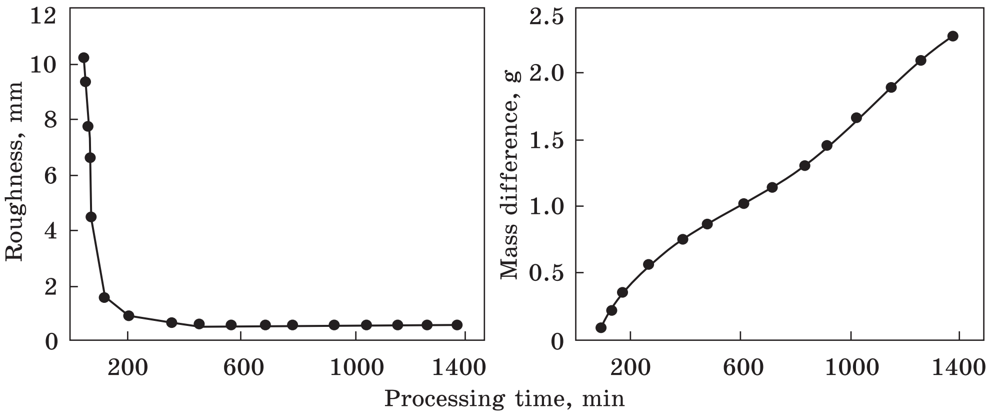

Fig. 16. Roughness and mass difference *vs.* processing time [47]

The results of the roughness change and mass abrasion during stream finishing as a function of machining time are shown in Fig. 16, *a*, *b*. The selected drum speed of 70 min^{-1} results in the significant surface improvement from $S_a \approx 10$ μm to $S_a \approx 0.3$ μm, which remains constant even at longer processing times. The best measurement result was $S_a = 0.32$ μm for the SFP specimen, while it was $S_a = 1.15$ μm for the turned specimens.

Figure 17 shows the S–N data points of the rotating bending fatigue test as well as the determined Wöhler curves of the as printed, the turned and the stream-finished samples. The inclination of the Wöhler lines is $k = 4.34$ for the as-printed samples, $k = 6.67$ for the turned samples and $k = 16.57$ for the stream-finished samples. The comparison of the determined Wöhler curves of the as-printed samples also shows the downward shift of the turned samples' curve. The data point for the stream-finished sample set at the stress amplitude of 60 MPa was not included in the determination of the Wöhler curves according to VDI 3405-2 and was marked as 'not evaluated'. The Wöhler curve of the stream-finished samples is significantly flatter. In the range of high cycle numbers, the stream-finished samples show higher fatigue strength than the turned samples. However, at cycle numbers below 10^5, the data points of the stream-finished

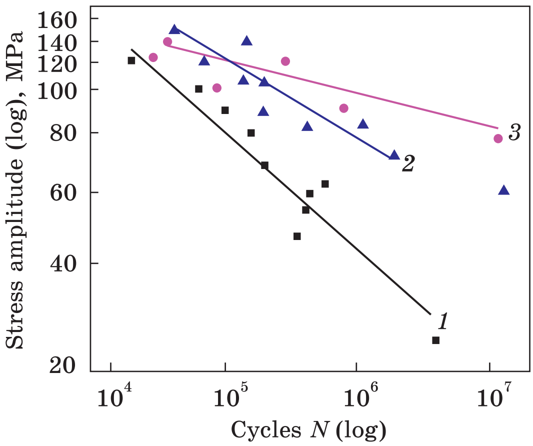

Fig. 17. The S–N data curves: *1* — as-printed; *2* — machined; *3* — stream-finished [47]

specimens are below those of the turned samples. Fatigue strength can be significantly increased compared to the as-printed samples. The closing of pores and the presumed introduction of compressive residual stresses during stream finishing, combined with reduced surface roughness, result in a flat Wöhler curve, which at high load cycles is well above the Wöhler curve of turned samples.

3.5. Shot-Peening

The effect of the shot peening (SP) on the fatigue resistance was investigated in [48]. The samples were printed using the continuous Yb fibre laser (λ = 1064 nm) with the power of 400 W and beam diameter between 100–150 μm, creating melt pools with dimensions of 300×150 μm. The scanning speed of the laser was 1 m/sec, and the hatching strategy involved 8 mm wide stripes that were scanned back and forth; the hatching distance was 200 μm with a 33% overlap; the layer thicknesses before and after melting were 60 and 30 μm, respectively; the printing rate was 7.4 mm^3/s. All samples were printed in the Z direction. The printing was conducted under an Argon atmosphere with the maximum oxygen content of about 0.12%. The temperature of a printing plate was 35 °C. To reduce residual stress, the samples printed underwent stress relief heat treatment (at 300 °C for 2 hours) and were machined to standard fatigue requirements (ASTM E466-96 standard) with a length of 80 mm, an inner diameter of 5 mm and a 50 mm gauge [49]. To perform SP, the two types of balls are used: steel balls and ceramic balls (Almen intensity I = 5″A and I = 12.2″ N for SP, which were used after the mechanical (MP) or electrolytic (EP) polishing, respectively). The fatigue tests up to failure were conducted at room temperature using the Moore rotating beam machine. The load (W) was applied using weights placed on hooks on the shoulders of the samples to create the constant torque. The stress amplitude was changed by adjusting the weights. The amplitude of the stress σ_a in the cylindrical samples with diameter D and length L was calculated as $\sigma_a = 16WL/\pi D^3$. The loading frequency and stress ratio $R = \sigma_{min}/\sigma_{max}$ were 50 Hz and 0.1, respectively.

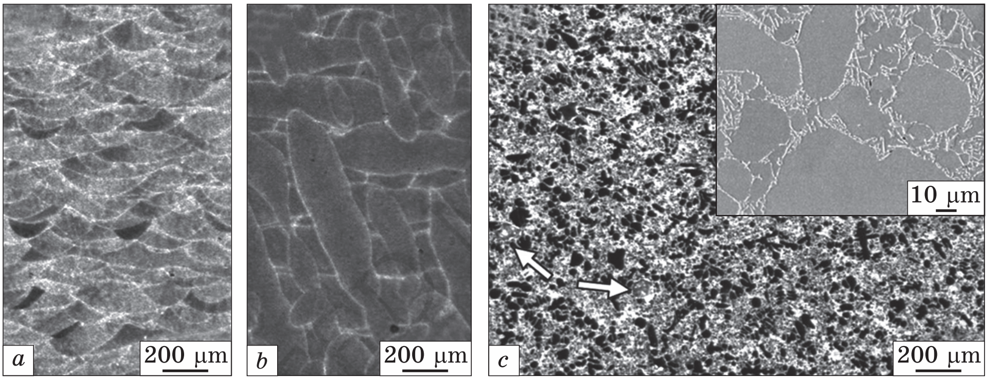

Fig. 18. Optical images of typical macrostructures: (*a*) AM-SLM, side-view; (*b*) AM-SLM, top-view; (*c*) die-cast alloy. Insert: SEM image at the higher magnification [47]

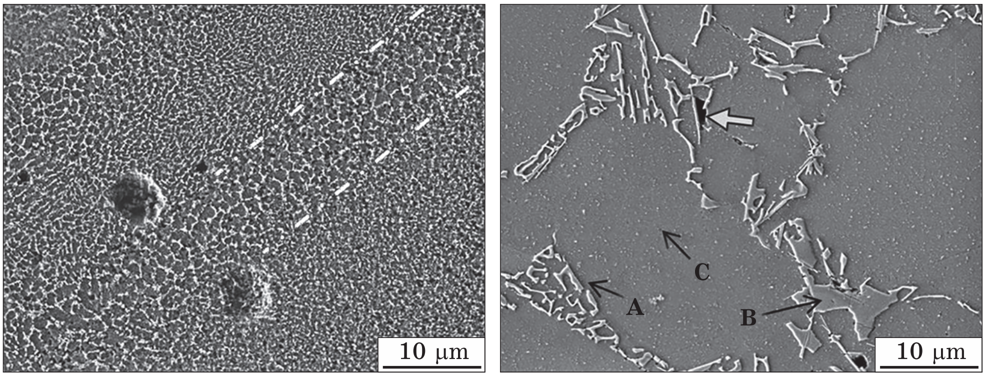

Fig. 19. HRSEM images of typical microstructures: (*a*) AM-SLM side/front-view; (*b*) die-cast sample [48]

Typical macrostructures of the side (X) and top (Z) of the printed and die-cast samples are presented in Fig. 18. The side-view of the printed sample (Fig. 18, *a*) reveals the 'fish scale' morphology of the macrostructure. The top-view (Fig. 18, *b*) shows track segments that reflect the rotation of the laser beam during printing. The macrostructure of the die-cast specimen (Fig. 18, *c*) displays the typical hypoeutectic structure of Al–Si cast alloy, with primary aluminium dendrites (dark regions) separated by inter-dendritic Al–Si eutectic. Large solidification defects marked by yellow arrows are observed.

The typical HRSEM microstructural image of AM-SLM specimens after stress relief treatment (Fig. 19, *a*) shows fine cellular eutectic morphology resulting from rapid solidification. A region with a relatively coarse microstructure is also observed (marked by red dashed lines). These regions are located at the boundaries of melt pools and contain a large fraction of relatively small pores, which probably formed as a result of

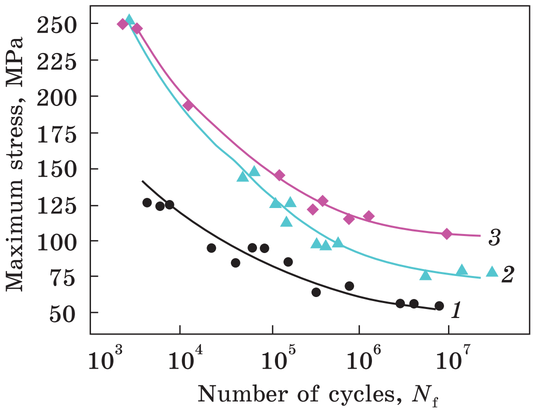

Fig. 20. The *S*–*N* curves: *1* — die-cast; *2* — no SP; *3* — SP steel balls [48]

shrinkage during solidification, when neighbouring regions had already solidified. The relatively large globular pores are mostly located within regions presenting the fine microstructure and are attributed to the entrapped inert gas. The HRSEM microstructure image of the die-cast specimen (Fig. 19, *b*) shows the relatively coarse solidification structure typical of hypo-eutectic Al-Si alloys, with needle-shaped eutectic Al–Si regions (*A*), homogeneously dispersed in the Al matrix (*B*), Fe-rich intermetallic phases (*C*) and observed solidification defects (yellow arrows). Similar findings are found in the literature [50].

The *S*–*N* curves for shot-peened samples after various surface treatments before SP are presented in Fig. 20. The maximal fatigue limit (S_f = = 110 MPa; $N_f = 10^7$) was achieved for shot-peened samples after polishing. The fatigue resistance of the samples shot-peened either by steel or ceramic balls turned out virtually the same. The lowest fatigue resistance was observed for die-cast samples. Optimal mechanical and electrochemical polishing of shot-peened surfaces that removed about 25–30 μm from the surface led to significant improvements in the fatigue resistance, especially for the high-cycle fatigue regime.

4. Conclusions

Among the aluminium–silicon–magnesium system, the widely recognised AlSi10Mg alloy has extensive applications in high-value-added products and has recently gained significant importance, notably in industries like aerospace and automotive due to its excellent strength-to-weight ratio, high thermal conductivity, and robust wear resistance. However, due to the low cooling rates of the cast processes and internal defects, traditional manufacturing processes produce the Aluminium alloy parts with coarse-grain microstructures, which are unsatisfactory for the industries provided with mechanical properties, particularly fatigue life of the engineering components. In the last few decades, to improve the performance properties of the AlSi10Mg alloy products, additive manufacturing has been successfully used for their production. AM permits the production of the metallic components and parts characterised by improved mechanical properties and complex shapes, which could hardly be obtained by conventional manufacturing processes. Among the AM techniques for metals, SLM is one of the most widely employed to produce aluminium-based parts, particularly of AlSi10Mg alloy, which is an attractive material for components in the high-performance industries, including aerospace, automotive, and electronics. SLM using the high-powered laser to melt and fuse powdered material layer by layer is particularly advantageous for producing complex components, as it enables the creation of lightweight parts with optimised shape, microstructure, and performance.

Fatigue resistance (performance) is an extremely important property for AlSi10Mg parts, particularly those used in industries where materials are subjected to cyclic loading repeated. Fatigue failure occurs when the metallic material gradually weakens under fluctuating stress, ultimately leading to fracture. Fatigue behaviour can be divided into the following three categories: 1) the high-cycle fatigue ($<10^4$ cycles); 2) the low-cycle fatigue ($<10^3$ cycles), and 3) the ultra-low-cycle fatigue (typically exceeding 10^7 or even 10^9 cycles). The fatigue performance of the AM AlSi10Mg alloy parts has been studied extensively, with results showing that it is comparable to, and in some cases superior to, conventionally cast-manufactured ones. This favourable performance is attributed to the refined microstructure achieved during the rapid cooling rates in the SLM process, which, as a rule, includes refining the cellular structure and increasing the grain boundary density. These factors hinder the propagation of the microcracks under cyclic loading, making it more difficult for cracks to grow and ultimately increasing fatigue resistance, which distinguishes it from conventionally cast AlSi10Mg. However, after the SLM process, there are numerous imperfections in terms of the bulk microstructure and the surface quality in the as-printed samples, which could lead to deterioration of the mechanical properties, especially regarding fatigue behaviour. In this regard, the effects of the SLM process parameters and the post-processing methods on the fatigue properties have been deeply investigated to obtain improved material properties and reduce the negative effects of the printing-inherent and surface defects, as well as the anisotropic microstructure. In addition, printing directions and the typically high surface roughness of SLM parts have been considered to lead to a significant reduction in fatigue performance.

In the present review, the effects of the different post-treatments, including heat treatment, mechanical and chemical surface treatment, as well as their combination as hybrid treatments, on the microstructure and fatigue properties of the SLM AlSi10Mg alloy samples were demonstrated. Based on the obtained results, we can conclude as follows.

In most cases, the role of the heat treatment on the mechanical properties of the printed samples was characterised before and after a typical T6 regime. This treatment process involves the solution treatment at 540 °C for 8 hours, followed by quenching using water, and subsequent artificial ageing at temperatures of 160°C for 10 hours, with final air-cooling. It was shown that the T6 heat treatment contributes to improving the fatigue strength compared to the as-printed state by promoting microstructural homogenization, heat-affected zone elimination and interdendritic Si spheroidization, as well as the relief of residual stress.

• It was established that hot isostatic pressing at 520 °C and 100 MPa for 2 h led to a decrease in the volume fraction of pores and significantly increased fatigue resistance.

• The friction stir processing is a short-route solid-state processing technique with one-step processing that achieves microstructural refinement, densification, and homogeneity and improves the fatigue behaviour of the printed samples. The fatigue crack growth rate is decreased by an order of magnitude after such treatment.

• The main effect of the mass abrasion during stream finishing as a function of machining time is to strongly improve the morphology and reduce the roughness of the as-printed samples, and at the same time, the generation of compressive residual stresses with increasing the hardness in the surface layer. These effects are resulting in remarkably improved fatigue life.

• Surface layer grain refinement leading to the gradient microstructure was obtained after applying shot peening. This treatment, in addition, modified the surface morphology as well as hardened the surface layer and induced high compressive residual stresses. These effects led to significant improvements in fatigue resistance, especially for a high-cycle fatigue regime. A combination of heat treatment + shot peening with ceramic shots + electrochemical polishing had the highest effects on the fatigue life improvement, leading to fatigue life 414-times higher compared to the as-printed state.

• Such information can be useful for optimising the post-process to improve the overall performance of the AM parts in practical applications. In conclusion, mechanical surface treatments, as well as suitable heat treatment, were found to be significantly resourceful as post-processing techniques to enhance efficiently the functionality and performance of SLM AlSi10Mg parts for structural applications under dynamic loading.

Acknowledgements. This work was supported by the Ministry of Education and Science of Ukraine *via* the Grant ‘Scientific basis of ultrasonic impact and additive manufacturing technologies of highly loaded unmanned aerial vehicle (UAV) parts with improved range’ (State Reg. No. 0124U001001) and the National Academy of Sciences of Ukraine (State Reg. No. 0123U102368).

Authors’ Contributions. S.M.V. designed the review concept, collected and analysed the literature data regarding heat treatment and shot peening. B.M.M. collected and analysed data on printing-related anisotropy, hot isostatic pressing post-processing, and fatigue strength. Performed review & editing of the manuscript. M.O.V. analysed the reviewed literature and additive manufacturing methods and prepared the first draft of the manuscript. A.P.B. collected and analysed the literature data regarding friction stir processing and stream finishing post-processing. All authors approved the final version of the manuscript.

REFERENCES

1. A.F. Madayag, *Metal Fatigue: Theory and Design* (Wiley: 1968).
2. Y. Murakami, Metal Fatigue: *Effects of Small Defects and Nonmetallic Inclusions* (Academic Press: 2019).
3. R.I. Stephens, A. Fatemi, R.R. Stephens, and O. Henry, *Metal Fatigue in Engineering* (Wiley & Sons: 2001).
4. J. Schijve, *Int. J. Fatigue*, **25**: 679 (2003); https://doi.org/10.1016/S0142-1123(03)00051-3
5. L.P. Pook, *Metal Fatigue: What It Is, Why It Matters. Solid Mechanics and Its Applications* (Springer: 2007).
6. M.M. Mohammed, *Multidisciplinary Mater. Chronicles*, **1**: 49 (2024); https://doi.org/10.62184/mmc.jmmc110020245
7. M. Zimmermann, *Int. Mater. Rev.*, **57**: 73 (2012); https://doi.org/10.1179/1743280411Y.0000000005
8. L. Wagner, *Mater. Sci. Eng.* A, 263: 210 (1999); https://doi.org/10.1016/S0921-5093(98)01168-X
9. E. Celik, *Additive Manufacturing: Science and Technology* (De Gruyter: 2025).
10. R. Tyagi, R. Kumar, and N. Ranjan, *Tribological Aspects of Additive Manufacturing* (CRC Press: 2024).
11. I. Gibson, D. Rosen, B. Stucker, M. Khorasani, I. Gibson, D. Rosen, B. Stucker, and M. Khorasani, *Additive Manufacturing Technologies* (Springer Int. Publishing: 2021).
12. R. Singh and J. Paulo Davim, *Additive Manufacturing Applications and Innovations* (CRC Press: 2021).
13. N. Gordon, *Aluminum Alloys: Properties, Processes and Applications* (States Academic Press: 2022).
14. C. Robles Hernandez, J.M. Herrera Ramírez, and R. Mackay, *Al–Si Alloys, Automotive, Aeronautical, and Aerospace Applications* (Springer: 2017).
15. J.E. Gruzleski and B.M. Closset, *The Treatment of Liquid Aluminum–Silicon Alloys* (American Foundrymen's Society: 1990).
16. L.W Lin, Y.F. Fang, Y.X. Liao, G. Chen, C. Gao, and P. Z. Zhu, *Adv. Eng. Mater.*, **21**: 1801013 (2019); https://doi.org/10.1002/adem.201801013
17. L. Pezzato, M. Dabala, S. Gross, and K. Brunelli, *Surf. Coat. Technol.*, **404**: 126477 (2020); https://doi.org/10.1016/j.surfcoat.2020.126477
18. B. Gao, H. Zhao, L. Peng, and Z. Sun, *Micromachines*, **14**: 57 (2023); https://doi.org/10.3390/mi14010057
19. K. Kempen, L. Thij, J. Van Humbeeck, and J.-P. Kruth, *Phys. Proc.*, **39**: 439 (2012); https://doi.org/10.1016/j.phpro.2012.10.059
20. A.P. Burmak, S.M. Voloshko, S.I. Sidorenko, I.A. Vladymyrskyi, M.M. Voron, B.M. Mordyuk, and M.O. Vasylyev, Anisotropy of the microstructure and microhardness of the AlSi10Mg alloy fabricated by selective laser melting, *Metallofiz.*

Noveishie Tekhnol., **47**, No. 5: 473 (2025) (in Ukrainian);
https://doi.org/10.15407/mfint.47.05.0473
21. M. Tang and P.C. Pistorius, *Int. J. Fatigue*, **125**: 479 (2019);
https://doi.org/10.1016/j.ijfatigue.2019.04.015
22. S.R. Ch, A. Raja, R. Jayaganthan, N.J. Vasa, and M. Raghunandan, *Mater. Sci. Eng. A*, **781**: 139180 (2020);
https://doi.org/10.1016/j.msea.2020.139180
23. N.E. Uzan, R. Shneck, O. Yeheskel, and N. Frage, *Mater. Sci. Eng. A*, **704**: 229 (2017);
https://doi.org/10.1016/j.msea.2017.08.027
24. M.-S. Baek, R. Kreethi, T.-H. Park, Y.H. Sohn, and K.-A. Lee, *Mater. Sci. Eng. A*, **819**: 141486 (2021);
https://doi.org/10.1016/j.msea.2021.141486
25. J. Fiocchi, A. Tuissi, P. Bassani, and C.A. Biffi, *J. Alloys Compd.*, **695**: 3402 (2017);
https://doi.org/10.1016/j.jallcom.2016.12.019
26. M. Matušů, J. Papuga, J. Rosenthal, J. Šimota, L. Džuberová, and L. Beránek, *Proc. Struct. Integrity*, **57**: 327 (2024);
https://doi.org/10.1016/j.prostr.2024.03.035
27. O.E. Zasimchuk, M.G. Chausov, B.M. Mordyuk, O.I. Baskova, V.I. Zasimchuk, T.V. Turchak, and O. S. Gatsenko, Features of strain hardening of heterogeneous aluminium alloys to enhance the fatigue durability, *Prog. Phys. Met.*, **22**, No. 4: 619 (2021);
https://doi.org/10.15407/ufm.22.04.619
28. A.P. Burmak, M.M. Voron, S.M. Voloshko, S.I. Sydorenko, I.A. Vladymyrs'kyy, S.I. Konorev, B.M. Mordyuk, and M.O. Vasyl'yev, Influence of heat treatment on microstructure and mechanical properties of AlSi10Mg alloy fabricated by additive and casting technologies, *Metallofiz. Noveishie Tekhnol.*, **47**, No. 8: 827 (2025) (in Ukrainian);
https://doi.org/10.15407/mfint.47.08.0827
29. C.A. Rodopoulos, A.Th. Kermanidis, E. Statnikov, V. Vityazev, and O. Korolkov, *J. Mater. Eng. Perform.*, **16**: 30 (2007);
https://doi.org/10.1007/s11665-006-9004-0
30. Y.K. Gao, *Mater. Sci. Eng., A*, **528**: 3823 (2011);
https://doi.org/10.1016/j.msea.2011.01.077
31. B.N. Mordyuk, G.I. Prokopenko, Y.V. Milman, M.O. Iefimov, and A.V. Sameljuk, *Mater. Sci. Eng. A*, **563**: 138 (2013);
https://doi.org/10.1016/j.msea.2012.11.061
32. E. Maleki, S. Bagherifard, and M. Guagliano, *J. Mater. Res. Technol.*, **24**: 3265 (2023);
https://doi.org/10.1016/j.jmrt.2023.03.193
33. R.H. Liu, S.B. Xu, C. Xu, K.W. Sun, X. Ju, X. Yang, Y.F. Pan, J. Li, G.C. Ren, and L.D. Wang, *J. Alloys Compd.*, **1010**: 178124 (2025);
https://doi.org/10.1016/j.jallcom.2024.178124
34. X. Ma, 3R. Gao, S. Xu, K.W. Sun, X.Z. Hu, M. Wang, and J. Li, *J. Mater. Eng. Perform.*, **34**, 6159 (2025);
https://doi.org/10.1007/s11665-024-09526-z
35. S.M. Voloshko, A.P. Burmak, S.I. Sidorenko, I.A. Vladymyrskyi, M.A. Vasylyev, B.N. Mordyuk, M.M. Voron, and P.O. Gurin, Surface modification of additively manufactured AlSi10Mg alloy by sand blasting, *Metallofiz. Noveishie Tekhnol.*, **48** (2026) (in Ukrainian) (in press).
36. E. Brandl, U. Heckenberger, V. Holzinger, and D. Buchbinder, *Mater. Design*, **34**: 159 (2012);
https://doi.org/10.1016/j.matdes.2011.07.067

37. R. Kovacheva, *Praktische Metallographie*, **30**: 68 (1993);
https://doi.org/10.1515/pm-1993-300203
38. G. Qiana, Z. Jiana, Y. Qianc, X.G. Pana, X.F. Mac, and Y.S. Honga, *Int. J. Fatigue*, **138**: 105696 (2020);
https://doi.org/10.1016/j.ijfatigue.2020.105696
39. M. Matušů, K. Dimke, J. Šimota, J. Papuga, J. Rosenthal, V. Mára, and L. Beránek, *J. Mech. Sci. Technol.*, **37**: 7 (2023);
https://doi.org/10.1007/s12206-022-2110-6
40. R.F. Fernandes, J.S. Jesus, R. Branco, L.P. Borrego, J.D. Costa, and J.A.M. Ferreira, *Eng. Failure Anal.*, **169**: 109210 (2025);
https://doi.org/10.1016/j.engfailanal.2024.109210
41. R.S. Mishra, M.W. Mahoney, S.X. McFadden, N.A. Mara, and A.K. Mukherjee, *Scripta Mater.*, **42**: 163 (1999);
https://doi.org/10.1016/S1359-6462(99)00329-2
42. A.H. Feng and Z.Y. Ma, *Scripta Mater.*, **56**: 397 (2007);
https://doi.org/10.1016/j.scriptamat.2006.10.035
43. G. Cam, *Int. Mater. Rev.*, **56**: 1 (2011);
https://doi.org/10.1179/095066010X12777205875750
44. A. Mishra, *Int. J. Res. Appl. Sci. Eng. Technol.*, **6**, No. 1: 1551 (2018);
http://dx.doi.org/10.2139/ssrn.3104223
45. M.M. El-Rayes and E.A. El-Danaf, *J. Mater. Proc. Technol.*, **212**: 1157 (2012);
https://doi.org/10.1016/j.jmatprotec.2011.017
46. J.G. Santos Macías, C. Elangeswaran, L. Zhao, J.-Y. Buffière, B. Van Hooreweder, and A. Simar, *Mater. Design*, **210**: 110084 (2021);
https://doi.org/10.1016/j.matdes.2021.110084
47. H. Wexel, S. Kramer, J. Schubert, V. Schulze, and F. Zanger, *Proc. CIRP*, **123**: 173 (2024);
https://doi.org/10.1016/j.procir.2024.05.032
48. N.E. Uzan, S. Ramati, R. Shneck, N. Frage, and O. Yeheskel, *Additive Manuf.*, **21**: 458 (2018);
https://doi.org/10.1016/j.addma.2018.03.030
49. L. Hitzler, J. Hirsch, B. Heine, M. Merkel, W. Hall, and A. Ochsner, *Materials*, **10**: 1136 (2017);
https://doi.org/10.3390/ma10101136
50. M.H. Lee, J.J. Kim, K.H. Kim, N.J. Kim, S. Lee, and E.W. Lee, *Mater. Sci. Eng. A*, **340**: 123 (2003);
https://doi.org/10.1016/S0921-5093(02)00157-0

Received / Final version
30.07.2025/ 22.01.2026

С.М. Волошко[1], *Б.М. Мордюк*[2], *М.О. Васильєв*[2], *А.П. Бурмак*[1]
[1] Національний технічний університет України
«Київський політехнічний інститут імені Ігоря Сікорського,
Берестейський просп. 37; 03056 Київ, Україна
[2] Інститут металофізики ім. Г.В. Курдюмова НАН України,
бульв. Академіка Вернадського, 36; 03142 Київ, Україна

МІКРОСТРУКТУРА ТА ВТОМНА ПОВЕДІНКА ЗРАЗКІВ СПЛАВУ AlSi10Mg, ВИГОТОВЛЕНИХ СЕЛЕКТИВНИМ ЛАЗЕРНИМ ТОПЛЕННЯМ

В огляді поєднано сучасні дослідження плаву AlSi10Mg і зосереджено увагу на зразках, одержаних методом селективного лазерного топлення (СЛТ). Наразі СЛТ є найперспективнішим серед нових технологій адитивного виробництва, що використовуються для друку деталей зі сплаву AlSi10Mg у промислових застосуваннях, таких як аерокосмічна й автомобільна промисловості. Більш конкретною метою цього дослідження є аналіз того, як параметри друку та методи постоброблення впливають на втому зразків зі сплаву AlSi10Mg, надрукованих методом СЛТ, для поліпшення якості продукції в умовах впливу вібрацій різних частот й інтенсивностей. Важливо зазначити, що характеристики втоми деталей, виготовлених методом СЛТ, оцінюються відповідно до відносних критеріїв об'ємної й поверхневої мікроструктур та дефектів. Проаналізовано такі параметри друку: потужність лазера, товщина шару, швидкість сканування, відстань штрихування, температура платформи й орієнтація друку. Розглянуто також методи постоброблення, що підвищують стійкість до втоми. До них належать термічне оброблення (зміцнення старінням і зняття напружень), оброблення тертям з перемішуванням, гаряче ізостатичне пресування, процес потокового оздоблення та дробоструминне зміцнення. Порівняно втомну поведінку зразків після друку та поверхневого модифікування. Критично обговорено вплив цих оброблень на мікроструктуру сплаву, зокрема розподіл і морфологію фаз Si в алюмінієвій матриці, оскільки вони впливають на втому.

Ключові слова: адитивне виробництво, мікроструктура, втома, алюмінієві сплави, селективне лазерне топлення.

 ISSN 1608-1021. Prog. Phys. Met., 2026, Vol. 27, No. 1